



Cr-doping regulates Mn_3O_4 spinel structure for efficient total oxidation of propane: Structural effects and reaction mechanism determination

Chao Feng^{a,b}, Chong Chen^a, Gaoyan Xiong^a, Di Yang^b, Zhong Wang^b, Yuan Pan^{a,*},
Zhaoyang Fei^c, Yukun Lu^a, Yunqi Liu^{a,*}, Runduo Zhang^d, Xuebing Li^{b,*}

^a State Key Laboratory of Heavy Oil Processing, College of Chemistry and Chemical Engineering, China University of Petroleum (East China), Qingdao 266580, China

^b Key Laboratory of Biofuels, Qingdao Institute of Bioenergy and Bioprocess Technology, Chinese Academy of Sciences, Qingdao 266101, China

^c State Key Laboratory of Materials-Oriented Chemical Engineering, Nanjing Technology University, Nanjing 211816, China

^d State Key Laboratory of Chemical Resource Engineering, Beijing Key Laboratory of Energy Environmental Catalysis, Beijing University of Chemical Technology, Beijing 100029, PR China

ARTICLE INFO

Keywords:

Cr- Mn_3O_4 spinel
Propane oxidation
Element doping
Volatile organic compounds
Reaction mechanism

ABSTRACT

The exploration of enhancing the low-temperature oxidation performance of catalysts by element doping is desirable but still challenging. Herein, a series of Cr-doping Mn_3O_4 spinel catalysts ($\text{Mn}_x\text{Cr}_{3-x}\text{O}_4$) were prepared through MOF-74 as precursors and tested for propane total oxidation. Due to the synergy between Cr and Mn, $\text{Mn}_x\text{Cr}_{3-x}\text{O}_4$ with rich surface-active Mn^{4+} , notable low-temperature reducibility and excellent oxygen migration capability displays notable catalytic activity for propane oxidation. The constructed $\text{Mn}_{2.70}\text{Cr}_{0.30}\text{O}_4$ exhibited superior propane catalytic activity and notable thermal stability. The T_{90} of $\text{Mn}_{2.70}\text{Cr}_{0.30}\text{O}_4$ is 264 °C under humid condition, that 51 °C lower than that of Mn_3O_4 . Meanwhile, in-situ spectroscopy and DFT calculations revealed that the addition of Cr can convert propane into propylene in the initial stage thus to reduce the reaction energy barrier. This work provides an element doping strategy to effectively enhance spinel catalysts performance, and can be provided with bright prospect for efficient VOCs catalysts.

1. Introduction

Volatile organic compounds (VOCs), especially short chain alkane, are the main precursors for ozone formation, haze and photochemical smog, that have compromised atmosphere and human health [1]. Propane is a representative short chain alkane mainly emitted from refineries, various industrial processes and automobile exhaust [2]. Because of its relatively stable C-H bond structure, it is usually used as a model molecule to evaluate catalyst performance [3]. Thus, the development of an efficient and stable degradation technology that conduct the total oxidation of propane is highly desirable [4]. The catalytic oxidation technology is the most suitable method of VOCs elimination for industrial requirement, due to the economic feasibility, high efficiency and harmless secondary pollutants [5]. Thus, it is critically significant to develop high active and cost-effective catalysts for controlling propane and reducing its impact on the environment [6].

Mn_3O_4 spinel catalyst, as promising transition metal oxide, have been widely used in light alkanes elimination, because of its economic efficiency and highly activity [7]. However, compared to noble metals

and cobalt oxides, the activity of Mn_3O_4 spinel catalyst required a further promotion [8,9]. Therefore, various strategies as morphology preparation, defect engineering and element doping have been used to enhance its low-temperature performance [10]. Wherein, by introducing a second elemental component into the catalyst, atom doping can adjust the characteristics of Mn_3O_4 spinel catalyst and improve its adsorption and catalytic performance [11]. As reported in the literatures, the incorporation of metal elements Co [12], Ni [13], La [14], Nb [7], Ce [15] into manganese-based oxides has a remarkably promotional effect on propane oxidation activity. Although Cr-doped catalysts are rarely reported, they have good propane dehydrogenation performance that widely used in propane catalytic production of propylene [16]. Meanwhile, Cr-dopant could form spinel high-entropy oxides, improve in charge carrier properties and display higher lattice oxygen transfer performance [17]. Therefore, the introduction of Cr can better realize the catalytic oxidation of propane at low temperature and enhance the catalytic activity of the Mn_3O_4 spinel catalyst.

Controllable and effective element doping technology plays an important role in the structure and properties of catalytic materials. The

* Corresponding authors.

E-mail addresses: panyuan@upc.edu.cn (Y. Pan), liuyq@upc.edu.cn (Y. Liu), lixb@qibebt.ac.cn (X. Li).

<https://doi.org/10.1016/j.apcatb.2023.122528>

Received 30 September 2022; Received in revised form 9 January 2023; Accepted 23 February 2023

Available online 24 February 2023

0926-3373/© 2023 Elsevier B.V. All rights reserved.

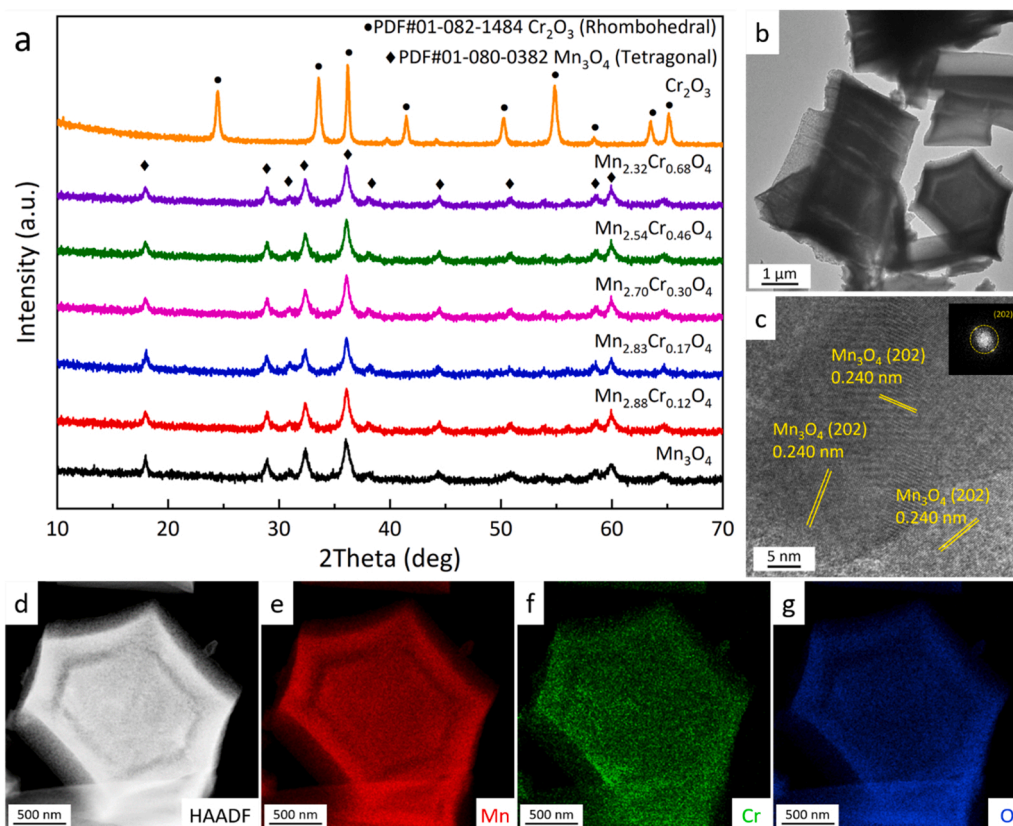


Fig. 1. (a) Powder XRD patterns of $\text{Mn}_x\text{Cr}_{3-x}\text{O}_4$ catalysts, (b) TEM and (c) HRTEM images and (d-g) elemental mapping of the $\text{Mn}_{2.70}\text{Cr}_{0.30}\text{O}_4$ catalyst.

traditional synthesis strategies, such as sol-gel method [18], co-precipitation method [19] and impregnation method [20], have disadvantages in poor dispersion, uneven particle size, unclear loading and easy migration of active sites. Instead, with metal organic framework material (MOF) as the precursor, the metal oxide can improve the dispersion through the coordination network structure of MOF [21]. Also, the presence of organic frameworks can limit the range of metal sites, enabling precise regulation of active sites through clear coordination states [22].

Herein, Cr-doped $\text{Mn}_x\text{Cr}_{3-x}\text{O}_4$ spinel catalysts were synthesized using bimetallic MnCr-MOF-74 as precursor, aiming at improving the activity of Mn_3O_4 spinel catalyst for propane total oxidation. Different degrees of element doping were adjusted by the content of Cr doping. And the effect of Cr doping on catalyst properties was investigated by characterization and performance evaluation. Simultaneously, in-situ diffuse reflectance infrared Fourier transform spectra (in-situ DRIFTS) and density functional theory (DFT) techniques were investigated to interpret the adsorption, activation behaviors and possible reaction mechanism. This study provides an element doping mechanism that can effectively activate and enhance the oxidation performance of spinel catalysts.

2. Experimental

2.1. Catalyst preparation

Synthesis of MnCr-MOF-74 . MnCr-MOF-74 was synthesized following a hydrothermal method [23]. In a typical procedure, “y mmol” $\text{Mn}(\text{NO}_3)_2 \cdot 4 \text{H}_2\text{O}$ (Aladdin, $\geq 99\%$) and “3-y mmol” $\text{Cr}(\text{NO}_3)_3 \cdot 9 \text{H}_2\text{O}$ (Aladdin, $\geq 99\%$) were dissolved in 50 mL of N,N-dimethylformamide, 5 mL of deionized water and 5 mL of ethanol. Then, 1.5 mmol 2,5-dihydroxyterephthalic acid was added with stirring to obtain a clear and homogeneous solution. Transfer the solution into a 100 mL autoclave.

The reaction was carried out at 120 $^\circ\text{C}$ for 24 h. Then, it was filtered, washed three times with deionized water and ethanol respectively, and dried in vacuum for 12 h to gain the product $\text{Mn}_y\text{Cr}_{3-y}\text{MOF-74}$.

Synthesis of $\text{Mn}_x\text{Cr}_{3-x}\text{O}_4$. The synthesized $\text{Mn}_y\text{Cr}_{3-y}\text{MOF-74}$ catalyst precursor was put into a tube furnace and heated to 600 $^\circ\text{C}$ at a rate of 2 $^\circ\text{C}\cdot\text{min}^{-1}$ in a nitrogen atmosphere, and the heating was continued for 3 h. After the tube furnace was cooled to room temperature, the nitrogen was turned off, the inlet of the tube furnace was opened, and the samples were slowly oxidized in air for 2 h. Then, the pyrolyzed samples were placed in a muffle furnace and calcined at 350 $^\circ\text{C}$ for 4 h. The sample was labeled $\text{Mn}_x\text{Cr}_{3-x}\text{O}_4$, where x was calculated with inductively coupled plasma atomic emission spectrometry (ICP-AES) measurement. The contents of Mn and Cr in the catalyst determined by ICP-AES, X-ray photoelectron spectroscopy (XPS) and energy-dispersive X-ray spectroscopy elemental mapping (EDS mapping) are listed in Table S1.

2.2. Catalyst characterization

Data obtained using the X-ray diffraction (XRD), the nitrogen adsorption-desorption isotherms, Raman spectroscopy, scanning electron microscopy (SEM), transmission electron microscopy (TEM), high-resolution transmission electron microscopy (HRTEM), EDS mapping, Mn and Cr K-edge X-ray absorption fine structure (XAFS) spectroscopy, XPS, electron paramagnetic resonance (EPR), ICP-AES, H_2 temperature-programmed reduction (H_2 -TPR), O_2 temperature-programmed desorption (O_2 -TPD), in-situ DRIFTS techniques are presented in the Supporting Information (SI).

2.3. Catalyst evaluation

The catalytic activities were determined via a U-shape bed quartz tube reactor with 200 mg of catalyst. The feed gas was 2500 $\mu\text{g}\cdot\text{g}^{-1}$ of

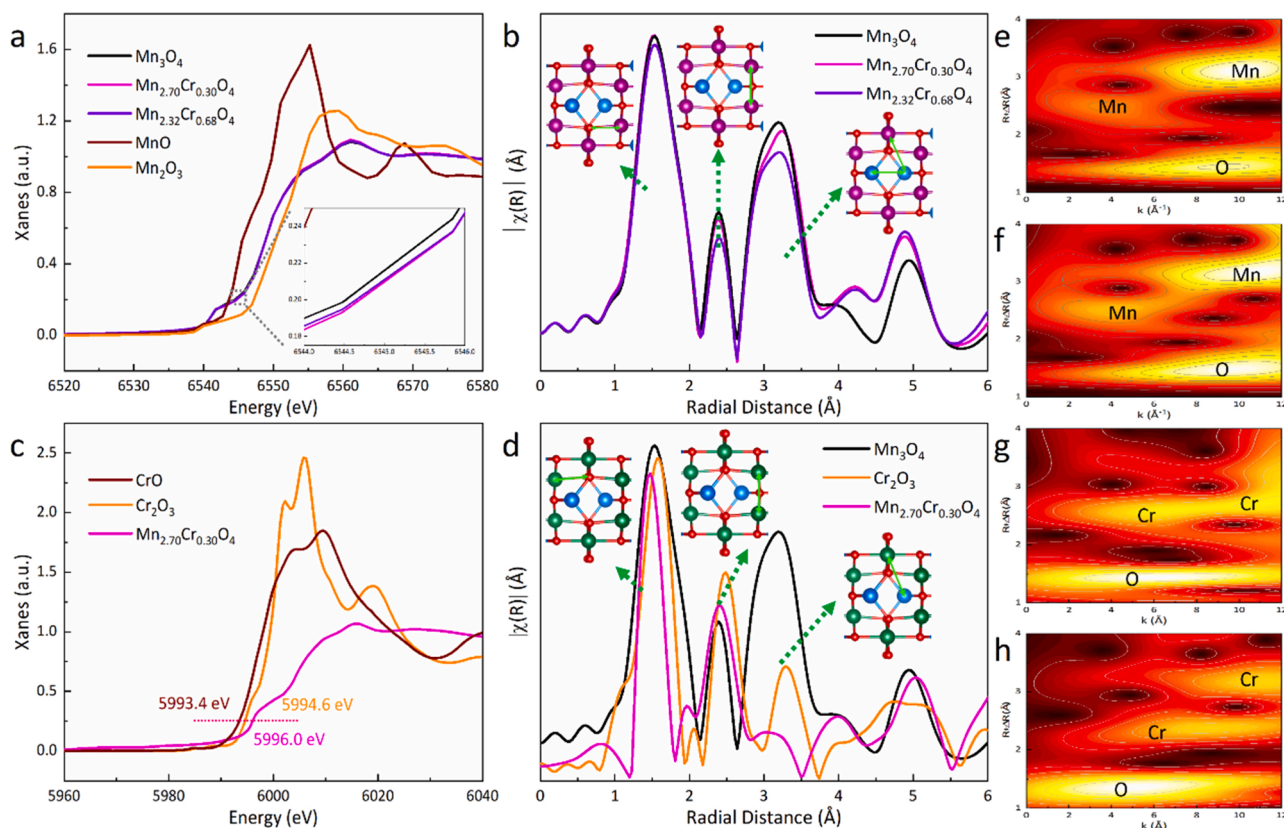


Fig. 2. (a) The Mn XANES and (b) the R-space FT EXAFS of $\text{Mn}_x\text{Cr}_{3-x}\text{O}_4$ catalysts Mn K-edge. (c) The Cr XANES and (d) the R-space FT EXAFS of $\text{Mn}_x\text{Cr}_{3-x}\text{O}_4$ catalysts Cr K-edge. WT plots at the Mn K-edge of (e) Mn_3O_4 , (f) $\text{Mn}_{2.70}\text{Cr}_{0.30}\text{O}_4$ and at the Cr K-edge of (g) $\text{Mn}_{2.70}\text{Cr}_{0.30}\text{O}_4$, (h) Cr_2O_3 .

C_3H_8 and air as the balance gas with a gas flow of $100 \text{ mL} \cdot \text{min}^{-1}$ (WHSV = $30000 \text{ mL} \cdot \text{g}^{-1} \cdot \text{h}^{-1}$). The detailed reaction conditions and reaction kinetics are shown in the SI.

2.4. DFT calculation details

DFT technique were carried out by the Vienna ab initio simulation package (VASP) [24]. The detailed model construction, calculation parameter setting, the definition and calculation details of oxygen vacancy formation energy and Gibbs free energy are presented in SI.

3. Results and discussion

3.1. Structural and textural characteristics

Scheme S1 shows the method of preparing Cr-doped Mn_3O_4 spinel catalyst by using bimetallic MnCr-MOF-74 as the precursor. Since Mn and Cr are transition metals and have similar atomic structures, both of them can be uniformly dispersed in MOF-74 as the metal sites [25]. XRD patterns (Fig. S1) indicates that the Cr-doped MOF-74 materials maintained the consistency of structure and morphology. The process of calcination under nitrogen is shown in the thermogravimetric analysis (Fig. S2). Due to the barrier effect of organic ligands, Mn and Cr would not agglomerate rapidly, but form fine nanoparticles, and form spinel structure after further calcination and oxidation [26].

The crystal structure of the spinel catalysts was detected using the XRD technique. All diffraction peaks of the $\text{Mn}_x\text{Cr}_{3-x}\text{O}_4$ catalysts could be attributed to the pure Mn_3O_4 spinel phases (PDF#80-0382) (Fig. 1a) [27], indicating that Cr was doped in the Mn_3O_4 spinel structure. Meanwhile, the lattice parameters of $\text{Mn}_x\text{Cr}_{3-x}\text{O}_4$ catalysts were slightly reduced after Cr doping (Table S2), for the reason that the ionic radius of Cr^{3+} (0.615 Å) is slightly smaller than that of Mn^{3+} (0.645 Å) and Mn^{2+}

(0.670 Å). Additionally, the smaller particle size and larger Brunauer-Emmett-Teller (BET) specific surface area (Table S2 and Fig. S3) of $\text{Mn}_x\text{Cr}_{3-x}\text{O}_4$ catalysts confirmed that the barrier effect indeed avoided particle agglomeration.

The morphologies of $\text{Mn}_x\text{Cr}_{3-x}\text{O}_4$ spinel catalysts were analyzed using the SEM and TEM techniques. Compared with the regular cubic structure of MnCr-MOF-74 (Fig. S4), $\text{Mn}_x\text{Cr}_{3-x}\text{O}_4$ catalysts displayed as uniform nanoparticles (Fig. S5). TEM images of $\text{Mn}_x\text{Cr}_{3-x}\text{O}_4$ catalyst presented the microstructure of hexagonal prism (Fig. 1b). All the $\text{Mn}_x\text{Cr}_{3-x}\text{O}_4$ catalysts exhibited lattice fringes with 0.240 nm (Fig. 1c and Fig. S6), corresponding to the (202) faces of Mn_3O_4 spinel phase [26]. The fast Fourier transform images indicated that the $\text{Mn}_x\text{Cr}_{3-x}\text{O}_4$ catalysts represented high crystallinity. Due to the dispersion of MOF precursors, analysis of both the small-sized (Fig. S7) and the large-sized (Fig. 1d-g and Fig. S8) elemental mapping images revealed that Mn and Cr were uniformly scattered on $\text{Mn}_x\text{Cr}_{3-x}\text{O}_4$ catalysts surface.

XAFS was used to accurately analyze the coordination structure of Mn ions in $\text{Mn}_x\text{Cr}_{3-x}\text{O}_4$ spinel catalysts. The X-ray absorption near edge structure (XANES) spectral curves of $\text{Mn}_{2.70}\text{Cr}_{0.30}\text{O}_4$ and $\text{Mn}_{2.32}\text{Cr}_{0.68}\text{O}_4$ were located between MnO and Mn_2O_3 (Fig. 2a), demonstrated that the Mn species possessed valence states between +2 and +3 [28]. Meanwhile, the adsorption edges of $\text{Mn}_x\text{Cr}_{3-x}\text{O}_4$ catalysts were quite identical to pure Mn_3O_4 , indicating that the Mn species in $\text{Mn}_x\text{Cr}_{3-x}\text{O}_4$ catalysts presented similar valence states to Mn_3O_4 . Analysis of the R-space Fourier-transformed (FT) ($k^3\chi(k)$) signified that major shells of $\text{Mn}_{2.70}\text{Cr}_{0.30}\text{O}_4$ and $\text{Mn}_{2.32}\text{Cr}_{0.68}\text{O}_4$ were located at $\sim 1.54 \text{ Å}$, $\sim 2.38 \text{ Å}$, and $\sim 3.20 \text{ Å}$ (Fig. 2b), which belong to the Mn-O, $\text{Mn}^{3+}\text{-Mn}^{3+}$ and $\text{Mn}^{2+}\text{-Mn}^{3+}$ (Mn^{2+}) coordination in the Mn_3O_4 octahedra, respectively [28]. Meanwhile, the peak positions of the Mn-Mn coordination in the second and third shell layer remained the same, indicating that Cr doping would not affect Mn coordination environment [29].

The K-edge XAFS of Cr element was measured to further determine

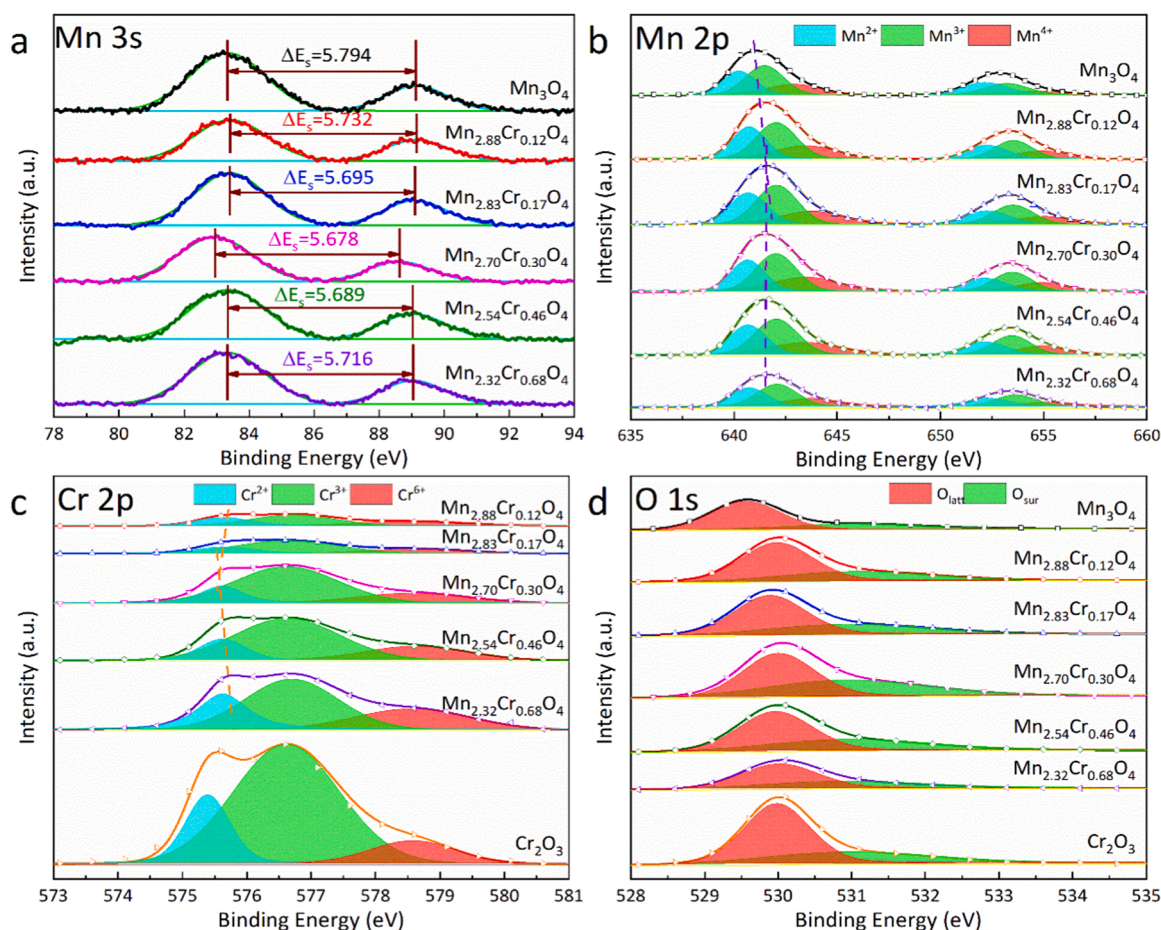


Fig. 3. XPS profiles of the $\text{Mn}_x\text{Cr}_{3-x}\text{O}_4$ catalysts: (a) Mn 3s, (b) Mn 2p, (c) Cr 2p and (d) O 1s.

the position of Cr ions in $\text{Mn}_x\text{Cr}_{3-x}\text{O}_4$ spinel catalysts. The Cr absorption edge energy of $\text{Mn}_{2.70}\text{Cr}_{0.30}\text{O}_4$ catalyst in XANES spectrum was higher than that of CrO and Cr_2O_3 (Fig. 2c), implying that the Cr species displayed a higher valence state than +3. Furthermore, three apparent shells could be observed in the R-space spectrum of $\text{Mn}_{2.70}\text{Cr}_{0.30}\text{O}_4$, situated at ~ 1.51 Å, ~ 2.38 Å, and ~ 3.19 Å (Fig. 2d), respectively. Compared with Cr_2O_3 , the doped Cr was closer to the Mn^{3+} coordination environment in Mn_3O_4 , signifying that Cr partially replaced the B site Mn^{3+} in spinel structure [30]. The peak position of Cr-O coordination shifted from 1.54 Å to 1.51 Å, due to the shorter Cr-O bond length [31]. However, the maintenance of the Mn_3O_4 spinel structure bulk phase made the Cr^{3+} -Mn coordination in the second and third shells hardly change. Comparing the wavelet transform plots of Cr_2O_3 , Mn_3O_4 and $\text{Mn}_{2.70}\text{Cr}_{0.30}\text{O}_4$ (Fig. 2e-h), similarly, the Cr-O and Cr-Mn scattering of $\text{Mn}_{2.70}\text{Cr}_{0.30}\text{O}_4$ tended to the Mn-O and Mn-Mn scattering in Mn_3O_4 spinel structure, instead of Cr-O and Cr-Cr in Cr_2O_3 .

3.2. Surface chemical properties

XPS technique was measured to analyze the surface elemental composition and chemical state of $\text{Mn}_x\text{Cr}_{3-x}\text{O}_4$ spinel catalysts. The Mn average oxidation state (AOS) on surface was obtained via analysis of Mn 3s curve (Fig. 3a) [32], which in the order of $\text{Mn}_{2.70}\text{Cr}_{0.30}\text{O}_4$ (2.56) > $\text{Mn}_{2.54}\text{Cr}_{0.46}\text{O}_4$ (2.55) > $\text{Mn}_{2.83}\text{Cr}_{0.17}\text{O}_4$ (2.54) > $\text{Mn}_{2.32}\text{Cr}_{0.68}\text{O}_4$ (2.51) > $\text{Mn}_{2.88}\text{Cr}_{0.12}\text{O}_4$ (2.50) > Mn_3O_4 (2.43) (Table S3). The XPS Mn 2p spectra displayed two parts, located at 641.6 eV and 653 eV (Fig. 3b), which can be attributed to Mn 2p_{3/2} and 2p_{1/2} orbital [3], separately. The Mn^{3+} content on the surface decreased due to the doping of Cr at B site of the spinel. The Mn 2p_{3/2} peaks gradually shifted to high binding

energies (BEs) with the increase of Cr content, indicating the electron transfer from Mn to Cr species [8]. And due to the charge synergy between Mn and Cr, the Mn^{4+} content raised. More surface Mn^{4+} is beneficial to build more active sites and enhances the adsorption and activation capacity for oxygen and propane [33].

The Cr 2p_{3/2} spectra could be deconvoluted into three peaks at 578.6 eV, 576.7 eV and 575.6 eV (Fig. 3c), which were assigned to Cr^{6+} , Cr^{3+} and Cr^{2+} [16], respectively. As shown by the synchrotron radiation results, Cr in the $\text{Mn}_x\text{Cr}_{3-x}\text{O}_4$ catalyst mainly existed in the form of Cr^{3+} . The Cr 2p_{3/2} peaks gradually shifted toward low BEs with increasing of Cr contents. This observation is in good agreement with Fig. 5b, further suggesting that the Mn-Cr interaction results in the charge transfer between the Mn and Cr species [8]. Moreover, the high surface Cr^{6+} species in the $\text{Mn}_x\text{Cr}_{3-x}\text{O}_4$ catalyst affected as an oxygen storage body to stabilize the high valence state of Mn and Cr, so as to strengthen the catalyst oxidation capacity [16].

The properties of lattice oxygen (O_{latt}) and surface adsorbed oxygen (O_{sur}) could be deduced by peaks at 529.5 eV and 531.5 eV of the O 1s profiles (Fig. 3d) [34]. Compared with pure Mn_3O_4 and Cr_2O_3 , $\text{Mn}_x\text{Cr}_{3-x}\text{O}_4$ spinel catalysts displayed a higher content of O_{sur} , indicating that the lattice distortion caused by Cr-doping generated more surface defects as sites, where oxygen molecules are adsorbed and dissociated into surface active oxygen species [35].

For investigating the Cr doping effect on surface chemical bond properties, Raman spectrum were measured. The peak positions of $\text{Mn}_{2.83}\text{Cr}_{0.17}\text{O}_4$ were basically consistent with Mn_3O_4 spinel structure (Fig. 4a). The absorption peaks around 638 cm^{-1} , 284 cm^{-1} and 347 cm^{-1} could be attributed to the symmetrical vibration peak $\text{A}_{1g}(\nu_s)$ of Mn-O bond, the t_{2g} and E_g vibrational peaks of the asymmetric

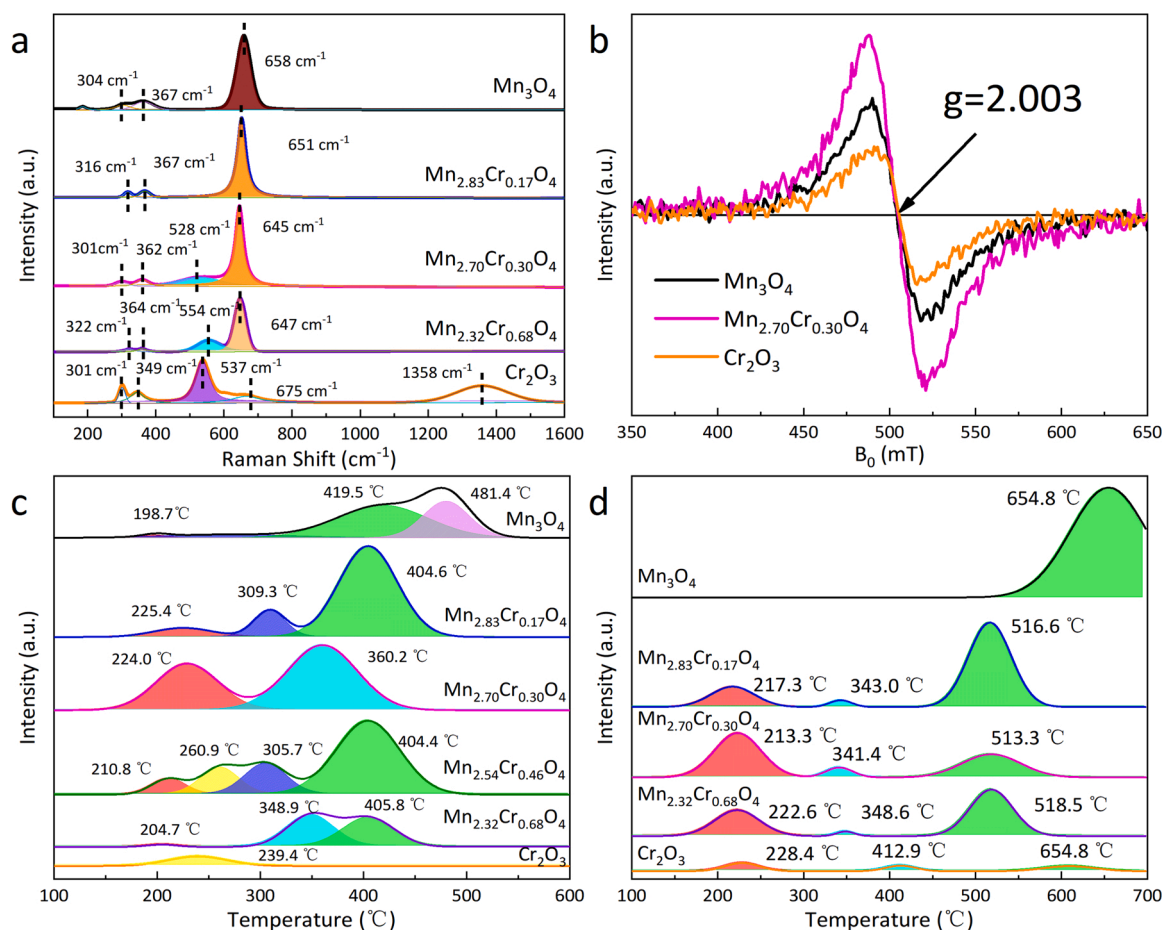


Fig. 4. (a) Raman spectral, (b) EPR spectral curves, (c) H_2 -TPR experiments, and (d) O_2 -TPD experiments over the $\text{Mn}_x\text{Cr}_{3-x}\text{O}_4$ catalysts.

stretching of the Housmannite model of Mn-O-Mn [36], separately. However, with the increase of Cr doping content, characteristic peaks at 550 cm^{-1} , belonging to Cr-O bonds, were detected in $\text{Mn}_{2.70}\text{Cr}_{0.30}\text{O}_4$ and $\text{Mn}_{2.32}\text{Cr}_{0.68}\text{O}_4$. And no vibration peak of Cr_2O_3 crystal phase at 1358 cm^{-1} was observed in all $\text{Mn}_x\text{Cr}_{3-x}\text{O}_4$ catalysts [37]. In addition, a blue shift in the position of the symmetrical vibrational peak of Mn-O was observed in $\text{Mn}_x\text{Cr}_{3-x}\text{O}_4$ catalysts, implying that Cr-doping led to a decrease in the force constant (k) (calculated following Hooke's law) [38] of the surface Mn-O bond (Fig. S9). The lower force constant also signified that the stretching vibration on surface of $\text{Mn}_x\text{Cr}_{3-x}\text{O}_4$ was relatively weak, meaning that the weaker chemical bond strength and easier to break for defects generation.

EPR spectra was analyzed to research the formation capacity of oxygen vacancies. The signal located at $g = 2.003$ represents the superoxide anion (O_2^-) on surface [39], indicating the concentration of surface oxygen vacancies. On account of the difference in radius and bonding between Cr ions and Mn ions, $\text{Mn}_x\text{Cr}_{3-x}\text{O}_4$ exhibited a more remarkable axial sign (Fig. 4b), demonstrating that Cr doping was instrumental in the generation of oxygen vacancies on the surface of Mn_3O_4 spinel catalysts.

The redox capacity of the catalysts is tremendously affected by the existence of reactive oxygen species and can be assessed by H_2 -TPR experiment. Cr_2O_3 possessed a small reduction peak near $240\text{ }^{\circ}\text{C}$, which belongs to the reduction of Cr^{6+} [30]. And Mn_3O_4 displayed poor oxidizing ability, with the reduction peak of H_2 at $419\text{--}481\text{ }^{\circ}\text{C}$ (Fig. 4c), which corresponds to the reduction of Mn^{3+} to Mn^{2+} [40]. After a small amount of Cr was doped into the Mn_3O_4 spinel structure, the reduction peak position was notable reduced, that the Mn^{3+} to Mn^{2+} temperature was dropped to about $405\text{ }^{\circ}\text{C}$. Besides, due to the surface rich reactive oxygen species by Cr-doping, multiple reduction peaks between 200 and

$300\text{ }^{\circ}\text{C}$ appeared, corresponding to Mn^{4+} partly reduced to Mn^{3+} and reduction of Cr^{6+} to Cr^{3+} [41]. The quantitative result revealed $\text{Mn}_{2.70}\text{Cr}_{0.30}\text{O}_4$ sample exhibited the largest H_2 consumption at $300\text{ }^{\circ}\text{C}$ (Table S4), indicating that it preserved the largest number of active oxygen species and could express an excellent reducing ability at low temperature.

O_2 -TPD profiles was determined to recognize the oxygen species desorbed from the surface as a function of temperature. Compared to Mn_3O_4 , obvious physical ($100\text{--}250\text{ }^{\circ}\text{C}$) and chemical adsorption ($200\text{--}450\text{ }^{\circ}\text{C}$, $450\text{--}650\text{ }^{\circ}\text{C}$) of oxygen species could be observed in the $\text{Mn}_x\text{Cr}_{3-x}\text{O}_4$ catalyst (Fig. 4d), which was related to the introduction of Cr into the surface lattice distortion and the formation of a large number of oxygen vacancies [42]. Based on quantitative analysis, $\text{Mn}_{2.70}\text{Cr}_{0.30}\text{O}_4$ displayed the largest oxygen desorption amount at $300\text{ }^{\circ}\text{C}$ (Table S5), because of the more defects and oxygen vacancies on surface. The defects caused by Cr doping can strengthen the adsorption, activation ability of oxygen molecules and surface oxygen species migration ability, so that generate abundant active oxygen species at low temperature [33].

3.3. Catalytic performance evaluation

Total oxidation of propane evaluation of $\text{Mn}_x\text{Cr}_{3-x}\text{O}_4$ catalysts was performed, that only CO_2 were detected by refinery gas analysis (Table S6). Especially, $\text{Mn}_{2.70}\text{Cr}_{0.30}\text{O}_4$ performed better catalytic activity (Fig. S10, Table S7), even compared to other catalysts reported (Table S8), clarifying the fact that Cr-doping engineering is an effective modification method for oxidation catalyst fabrication.

$\text{Mn}_x\text{Cr}_{3-x}\text{O}_4$ catalysts also exhibited wonderful catalytic activity under humid condition. When 5 vol% water vapor was additional into

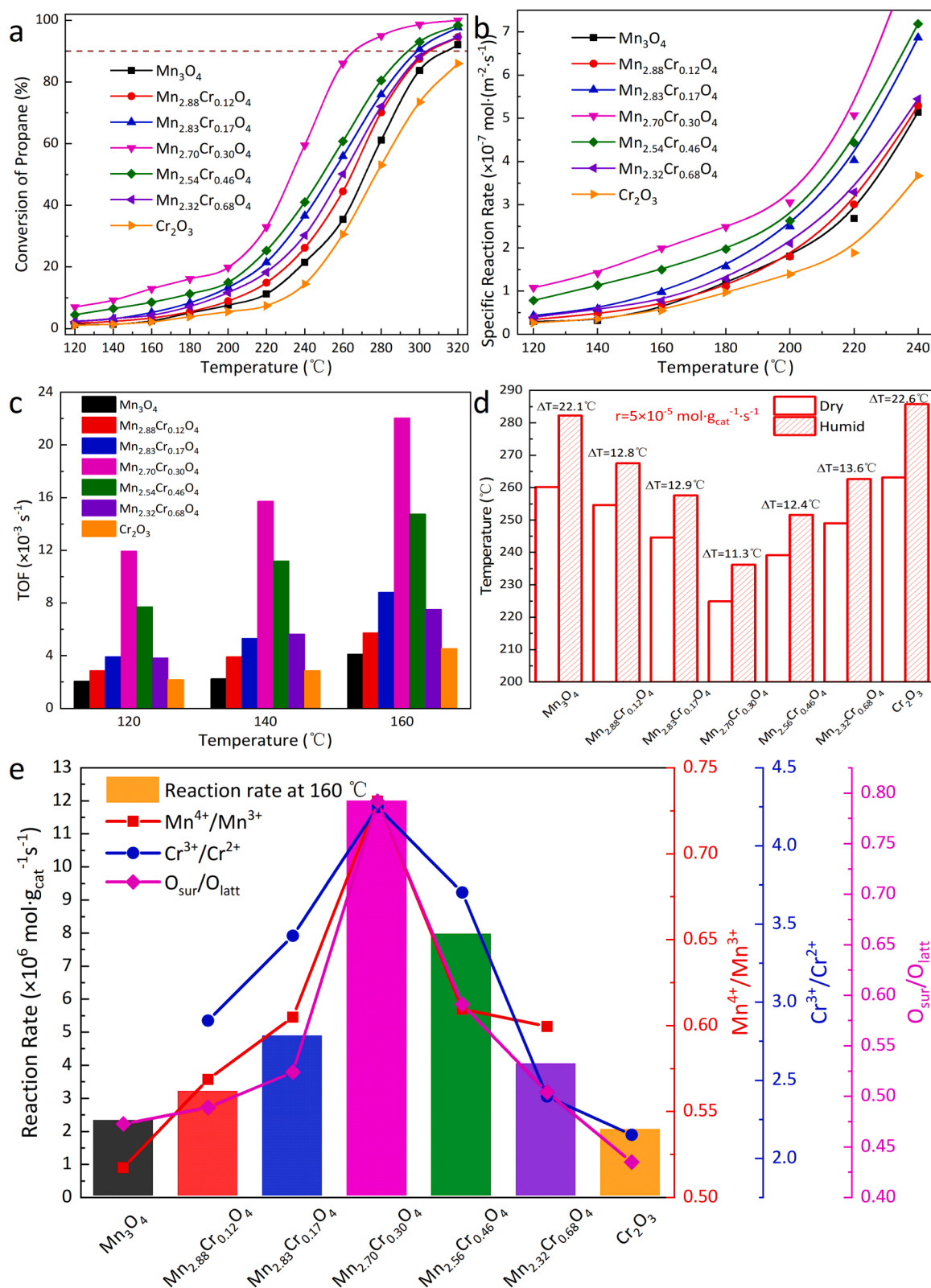


Fig. 5. (a) Activities, (b) SSA and (c) TOFs for propane total oxidation of $\text{Mn}_x\text{Cr}_{3-x}\text{O}_4$ catalysts under humid conditions. (d) Comparison of the reaction temperature of $\text{Mn}_x\text{Cr}_{3-x}\text{O}_4$ catalysts under dry and humid conditions, (e) Correlation between the reaction rates at 160 °C and the ratios of the surface species recorded for the $\text{Mn}_x\text{Cr}_{3-x}\text{O}_4$ catalysts. The feed gas was $2500 \mu\text{g} \cdot \text{g}^{-1} \text{ C}_3\text{H}_8 + 5\% \text{ vol} \cdot \text{H}_2\text{O} + \text{air}$, $\text{WHSV} = 30000 \text{ mL} \cdot \text{g}^{-1} \cdot \text{h}^{-1}$.

Table 1

Catalytic performances (T_{10} , T_{50} , T_{90} , R_{160} , TOF_{160}) of the $Mn_xCr_{3-x}O_4$ catalysts at humid condition.

Sample	T_{10} ($^{\circ}C$)	T_{50} ($^{\circ}C$)	T_{90} ($^{\circ}C$)	R_{160} $\times 10^{-6}$ (mol (g _{cat} s) ⁻¹)	TOF_{160} $\times 10^{-3}$ (s ⁻¹)
Mn ₃ O ₄	216	271	315	2.29	4.12
Mn _{2.88} Cr _{0.12} O ₄	205	264	305	3.17	5.74
Mn _{2.83} Cr _{0.17} O ₄	187	254	298	4.85	8.82
Mn _{2.70} Cr _{0.30} O ₄	145	233	264	12.00	22.05
Mn _{2.54} Cr _{0.46} O ₄	170	249	293	7.95	14.75
Mn _{2.32} Cr _{0.68} O ₄	193	260	303	4.01	7.52
Cr ₂ O ₃	229	277	—	2.01	4.53

the reaction gas, in order of the T_{90} values, the sequences of activities were Mn_{2.70}Cr_{0.30}O₄ > Mn_{2.54}Cr_{0.46}O₄ > Mn_{2.83}Cr_{0.17}O₄ > Mn_{2.32}Cr_{0.68}O₄ > Mn_{2.88}Cr_{0.12}O₄ > Mn₃O₄ > Cr₂O₃ (Fig. 5a). Cr-doping could significantly improve the catalytic activity of $Mn_xCr_{3-x}O_4$ spinel catalyst, that only 2.5 wt% doping could reduce T_{90} by 10 $^{\circ}C$ (Table 1). Additionally, comparing to the T_{90} of Mn₃O₄ (315 $^{\circ}C$), Mn_{2.70}Cr_{0.30}O₄ could achieve 90% of propane decomposition at 264 $^{\circ}C$, which is 51 $^{\circ}C$ lower. However, as the addition amount continued to increase, the propane activity decreased. The specific surface activity (SSA) was obtained to exclude the influence of the specific surface area. Mn_{2.70}Cr_{0.30}O₄ also displayed the highest SSA (Fig. 5b) and turnover frequency (TOF) (Fig. 5c) at multiple

temperatures, indicating that it possessed the best intrinsic activity. Besides, the propane catalytic consumption rate (R_{160}) of Mn_{2.70}Cr_{0.30}O₄ was 12.00×10^{-6} mol·g_{cat}⁻¹·s⁻¹ at 160 $^{\circ}C$ (Table 1), that was five time those of Mn₃O₄ and Cr₂O₃. Compare the temperature difference required to gain the same reaction rate (5×10^{-5} mol·g_{cat}⁻¹·s⁻¹); $Mn_xCr_{3-x}O_4$ catalysts ($\Delta T \approx 12$ $^{\circ}C$) exhibited more excellent water resistance than pure Mn₃O₄ and Cr₂O₃ ($\Delta T \approx 22$ $^{\circ}C$) (Fig. 5d).

The enhancement of catalytic activity by Cr-doping was mainly reflected in the active sites' adjustment and surface oxygen species activation. Due to the synergistic effect between Mn and Cr, the valence of Mn species was increased and more Mn⁴⁺-O active sites were generated, which was beneficial to capture and reduction of propane molecules (Fig. 5e). Meanwhile, the increase of Cr³⁺/Cr²⁺ provided more balanced pair to stabilize and promote the electron transfer ability of Mn⁴⁺/Mn³⁺, thus enhanced the oxidation of propane and intermediates. The H₂-TPR results also reveal that Mn₃O₄ spinel catalyst could produce stronger low-temperature reduction performance by Cr-doping activation. Simultaneously, the oxygen vacancies caused by Cr-doping distortion supplied sufficient adsorption capacity of the oxygen molecules. Thereby, the continuous conversion of reactive oxygen species was achieved and the lattice oxygen mobility was improved. It signifies that the reversible process Mn³⁺-□-Mn³⁺+O₂ ↔ Mn³⁺-□-Mn⁴⁺-O₂ ↔ O⁻-Mn⁴⁺-□-Mn⁴⁺+O⁻ could proceed readily [43], leading to an obvious rise in the propane oxidation activity.

Besides, we also investigated the influence of other atmospheres on the catalyst activity. Mn_{2.70}Cr_{0.30}O₄ also displayed outstanding stability

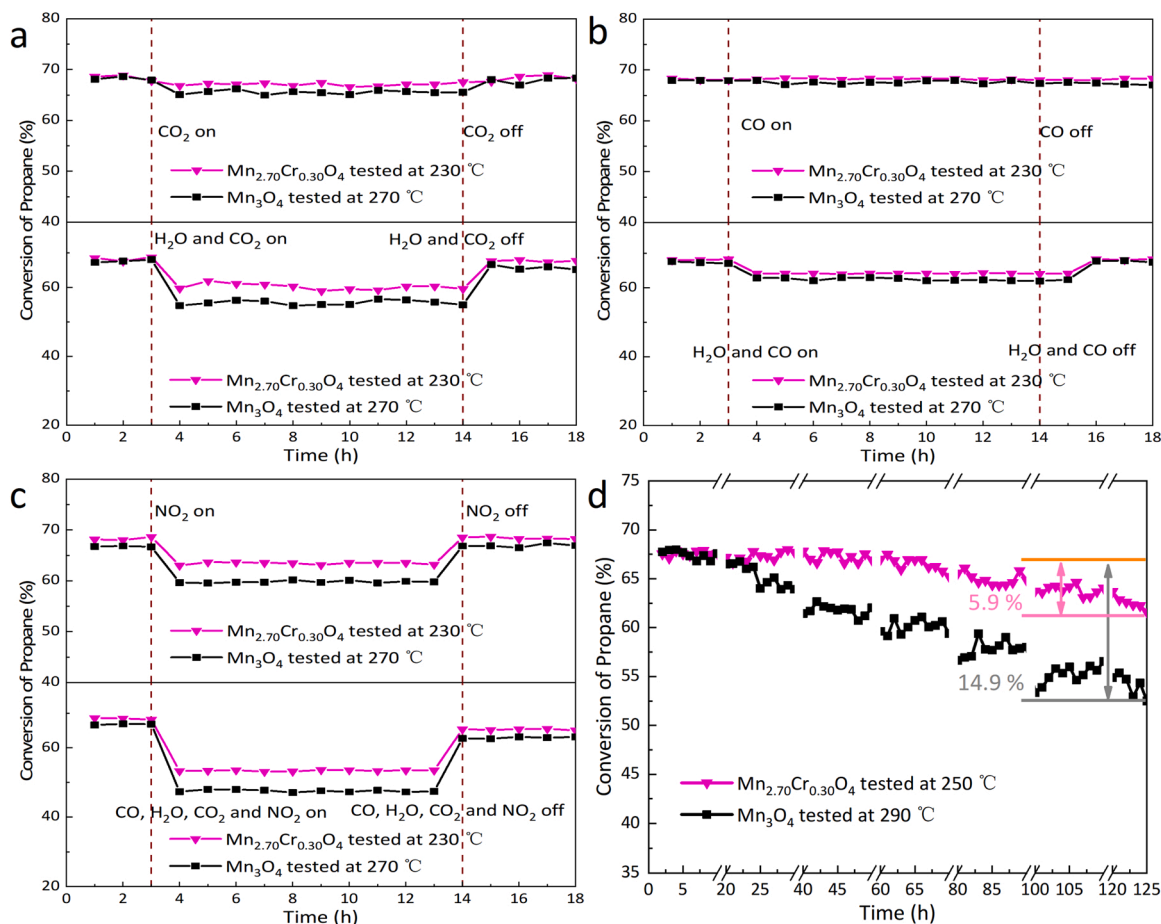


Fig. 6. (a) stability in the CO₂ and H₂O atmosphere of Mn_{2.70}Cr_{0.30}O₄ and Mn₃O₄ catalysts for propane oxidation. The feed gas was 2500 μg·g⁻¹ C₃H₈ + 5% vol. H₂O or 5 vol% CO₂ + air, WHSV = 30000 mL·g⁻¹·h⁻¹, (b) stability in the CO and H₂O atmosphere of Mn_{2.70}Cr_{0.30}O₄ and Mn₃O₄ catalysts for propane oxidation. The feed gas was 2500 μg·g⁻¹ C₃H₈ + 5% vol. CO₂ or/and 5 vol% H₂O + air, WHSV = 30000 mL·g⁻¹·h⁻¹, (c) stability in the NO₂ and complex atmosphere of Mn_{2.70}Cr_{0.30}O₄ and Mn₃O₄ catalysts for propane oxidation. The feed gas was 2500 μg·g⁻¹ C₃H₈ + 5% vol. CO, 5 vol% H₂O, 5 vol% CO₂ and 5 vol% NO₂ + air, WHSV = 30000 mL·g⁻¹·h⁻¹. (d) Long-term stability for propane oxidation of Mn_{2.70}Cr_{0.30}O₄ and Mn₃O₄ catalyst under humid condition.

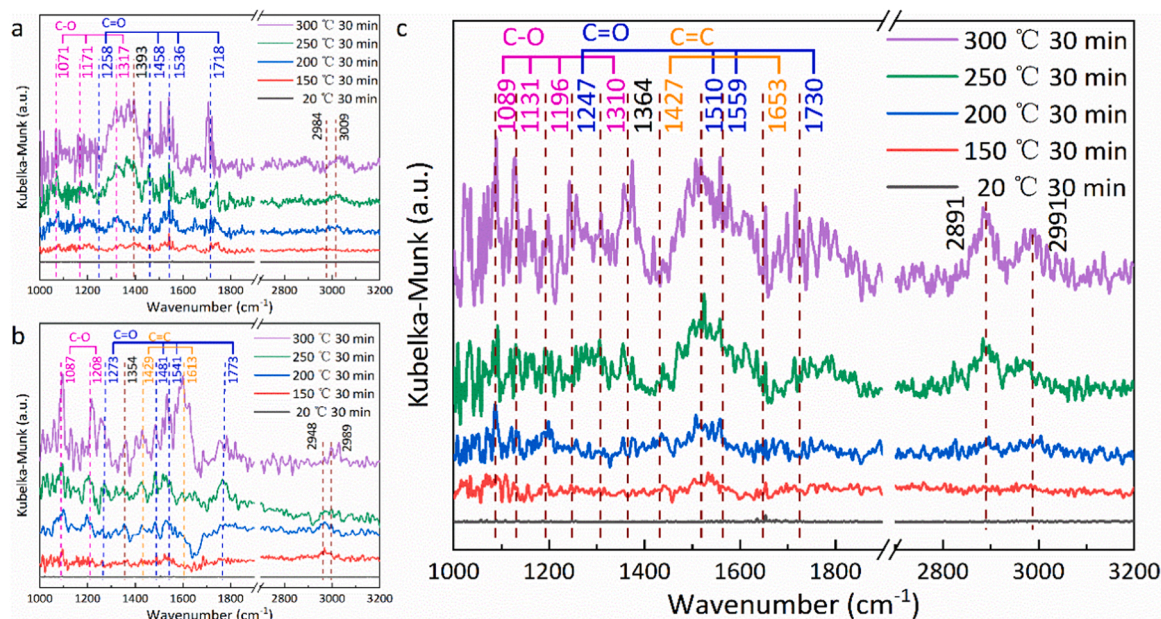


Fig. 7. Temperature-resolved *In-situ* DRIFT spectra of propane oxidation over (a) Mn_3O_4 , (b) Cr_2O_3 and (c) $\text{Mn}_{2.70}\text{Cr}_{0.30}\text{O}_4$ catalysts.

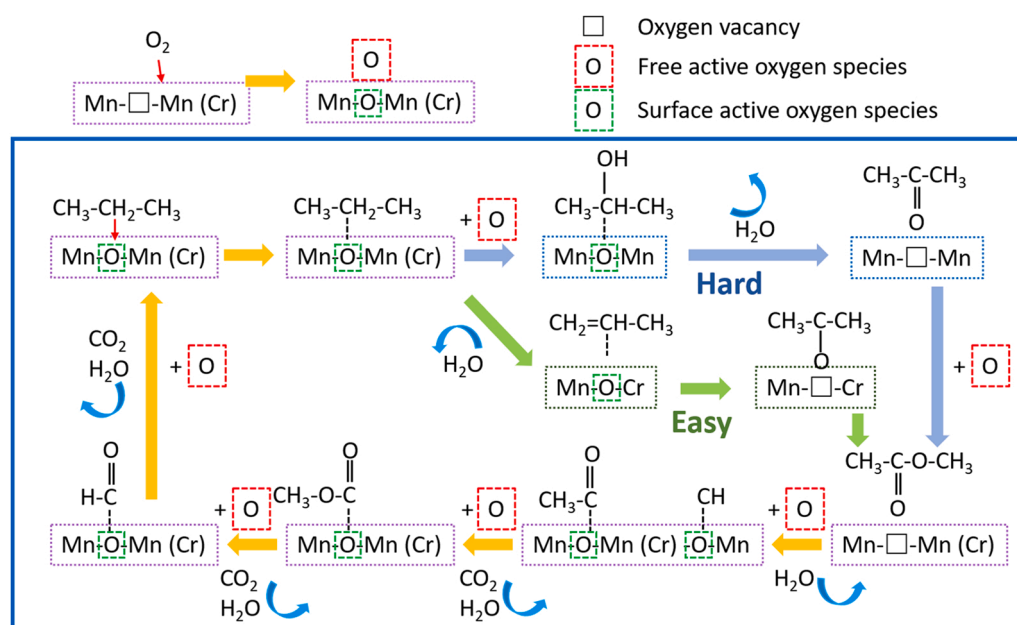
over 10 h with 5 vol% CO_2 added (Fig. 6a). When feed gas containing 5 vol% H_2O and 5 vol% CO_2 was introduced simultaneously, Cr-doped $\text{Mn}_{2.70}\text{Cr}_{0.30}\text{O}_4$ catalyst still exhibited stronger acid gas resistance. Compared with H_2O and CO_2 , the effect of CO on activity and stability could be almost ignored (Fig. 6b). Meanwhile, due to the reduction of CO , the H_2O resistance of the $\text{Mn}_{2.70}\text{Cr}_{0.30}\text{O}_4$ catalyst has been improved to a certain extent. Similarly, the effect of NO_2 was also weaker than H_2O (Fig. 6c), for the reason that NO_2 was only physically adsorbed on the surface in the form of gas. When the atmosphere complexity was adjusted to the maximum, $\text{Mn}_{2.70}\text{Cr}_{0.30}\text{O}_4$ catalyst could still maintained strong stability under the action of various atmosphere.

Stability experiments were detected to present the application prospect. The long-term stability experiment indicated that the high propane conversion of $\text{Mn}_{2.70}\text{Cr}_{0.30}\text{O}_4$ could preserve for more than 120 h under dry and humid conditions (Fig. S11, Fig. 6d) and almost

unaffected by space velocity (Fig. S12). Additionally, $\text{Mn}_{2.70}\text{Cr}_{0.30}\text{O}_4$ exhibited outstanding cycle stability during five cycles (Fig. S13), and remarkable thermal stability in high-low temperature switch experiment as well (Fig. S14). In term of structural stability, after the reaction, $\text{Mn}_{2.70}\text{Cr}_{0.30}\text{O}_4$ maintained the Mn_3O_4 spinel structure (Fig. S15) with (202) crystal face exposed (Fig. S16). Simultaneously, the surface elemental structure and chemical state of Mn and Cr did not show obvious changes after reaction (Fig. S17, Table S9), signifying the elemental composition was quite stable.

3.4. *In-situ* DRIFT spectroscopy

The temperature-resolved *in-situ* DRIFT spectra of Mn_3O_4 , Cr_2O_3 and $\text{Mn}_{2.70}\text{Cr}_{0.30}\text{O}_4$ catalysts were measured to intermediate the reaction mechanism of propane oxidation. When the reaction gas was adsorbed



Scheme 1. Proposed reaction pathway on $\text{Mn}_x\text{Cr}_{3-x}\text{O}_4$ catalyst for total oxidation of propane.

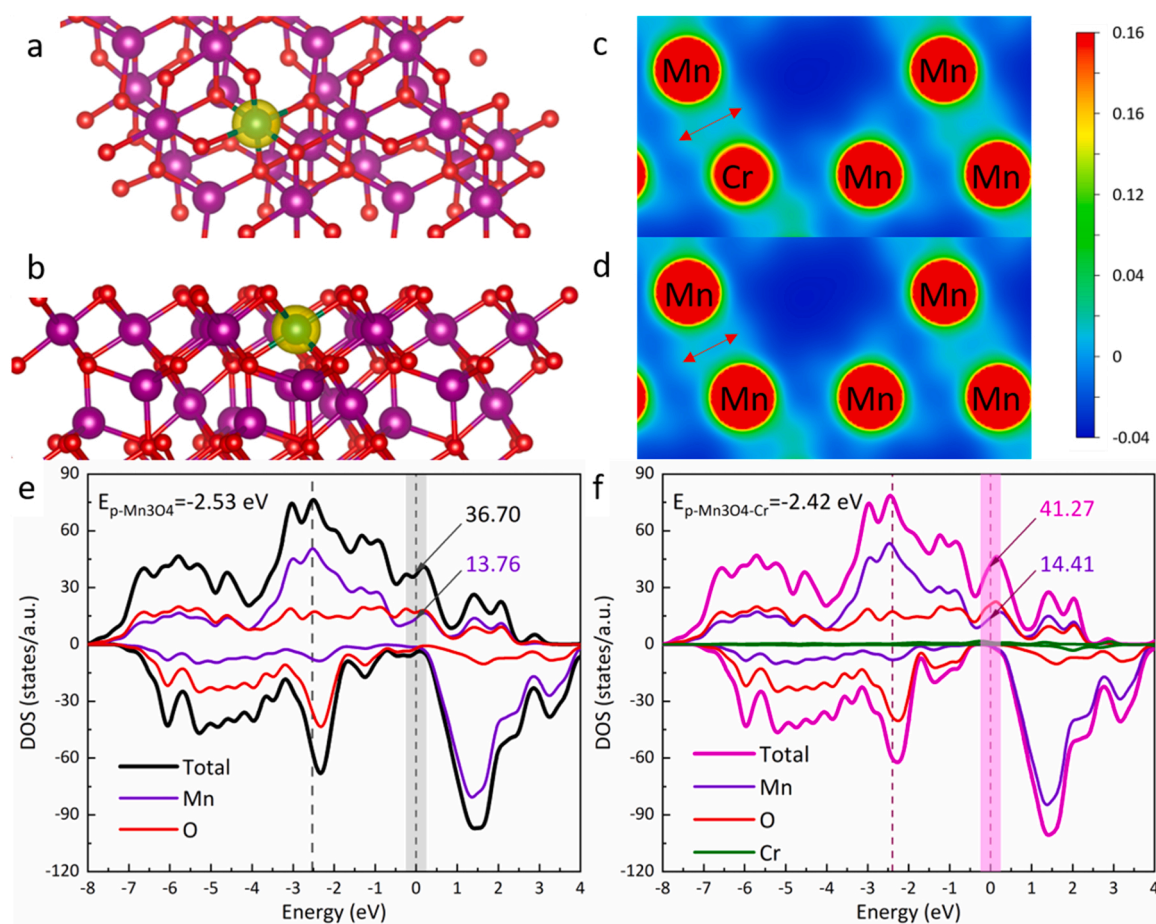


Fig. 8. Charge density difference plot for Cr doped Mn₃O₄ catalyst, view from (a) above and (b) side. The isosurface value is 0.0008 e-bohr⁻³. Yellow is positive and green is negative. Electron location function of Mn₃O₄ (c) before and (d) after Cr doping. Calculated PDOS of (e) Mn₃O₄ and (f) Cr-doped Mn₃O₄, the Energy equal zero represents the Fermi level (E_F).

on the surface of Mn₃O₄, vibrational peaks at 1393 cm⁻¹, 2984 cm⁻¹ and 3009 cm⁻¹ (Fig. 7a) were observed, which ascribed to the stretching vibration of CH₃ and CH₂ [44], signifying the adsorption of gaseous propane. Additionally, the absorption peaks appeared at 1258 cm⁻¹, 1458 cm⁻¹, 1536 cm⁻¹ and 1718 cm⁻¹, attributed to the vibrations of ν_s (C=O), ν_{as} (COO) and ν_s (CH₃COO) (Table S10). And the other absorption peaks at 1071 cm⁻¹, 1171 cm⁻¹ and 1317 cm⁻¹ were belonged to ν_s (C-O-CH), ν_{as} (C-O) and ν (C-O-C) vibration [45]. It indicates that the carbonate and carboxylate species were the main intermediates in the total oxidation of propane on the surface of Mn₃O₄. The vibrational peaks of Cr₂O₃ were basically the same as those of Mn₃O₄ (Fig. 7b), that the vibrational peaks of the C-O bond and C=O bond of the carboxylate could be obviously observed. However, adsorption peaks belonging to δ_{as} (CH₂) and ν_{as} (C=C) appeared in the reaction, were located at 1429 cm⁻¹ and 1623 cm⁻¹ [46], respectively. The enhancement of CH₂ asymmetric vibration and the appearance of C=C bond peak illustrated that olefin species are one of the transition products. According to the reports in the references [16,47], it can be inferred the reaction pathway that propane dehydrogenated to propylene and further complete oxidated to propane is existed.

The adsorption process of Mn_{2.70}Cr_{0.30}O₄ was similar to that of Cr₂O₃ (Fig. 7c), implying that the propylene, carbonate and carboxylate species are major intermediates. It indicated that two reaction paths were coexisted on Mn_{2.70}Cr_{0.30}O₄ surface (Scheme 1). The Gibbs free energy was calculated by DFT to verify the energy changes. The energy barrier for the formation of carbonyl intermediates via propylene was reduced to 0.76 eV (compared to 0.92 eV) and the Gibbs free energy curve was smoother (Fig. S18), illustrating that C-H bond was more prone to

fracture. Simultaneously, the C=C bond was easier to be oxidized and broken than C-C bond, indicating that the formation of propylene can enormously reduce the energy required of C₃ decomposed to C₂. In addition, more C-O peaks belonging to COO species could be detected, signifying that Cr-doping also enhanced the deep oxidation ability of intermediates. The change of reaction path and the enhancement of deep oxidation ability maximum strengthen the catalytic oxidation performance of propane.

3.5. Density function theory calculation

Analysis of the charge density difference plot was calculated by DFT to gain insight into the effect of Cr-doping on the electronic structure of Mn₃O₄ spinel catalyst. Due to the electricity-rich nature of Cr, the electron density around Cr increased when Cr³⁺ replaced Mn³⁺, indicating that more electrons could be transferred to adjust the charge of Mn and O (Fig. 8a,b) [48]. Simultaneously, the increase of electron cloud density between Mn and Cr certificated the existence of synergy (Fig. 8c,d). The bader charge analysis of Mn₃O₄-Cr shown that the valence electrons of Mn atoms around Cr are 11.188, 11.267, 11.259 and 11.383, which were lower than those of Mn₃O₄ (11.225, 11.229, 11.229, 11.229 and 11.449) (Fig. S19, Table S11). It implied that due to the electronic localization effect caused by Cr-doping, Mn atoms on surface own higher valence state. Moreover, density of states (DOS) was analyzed for surface properties. The DOS and Mn projected density of states (PDOS) near Fermi level (E_F) raised after Cr doping, implying the improvement of surface conductivity, effective electron transport and ion diffusion characteristics (Fig. 8e,f). Meanwhile, the DOS peak of

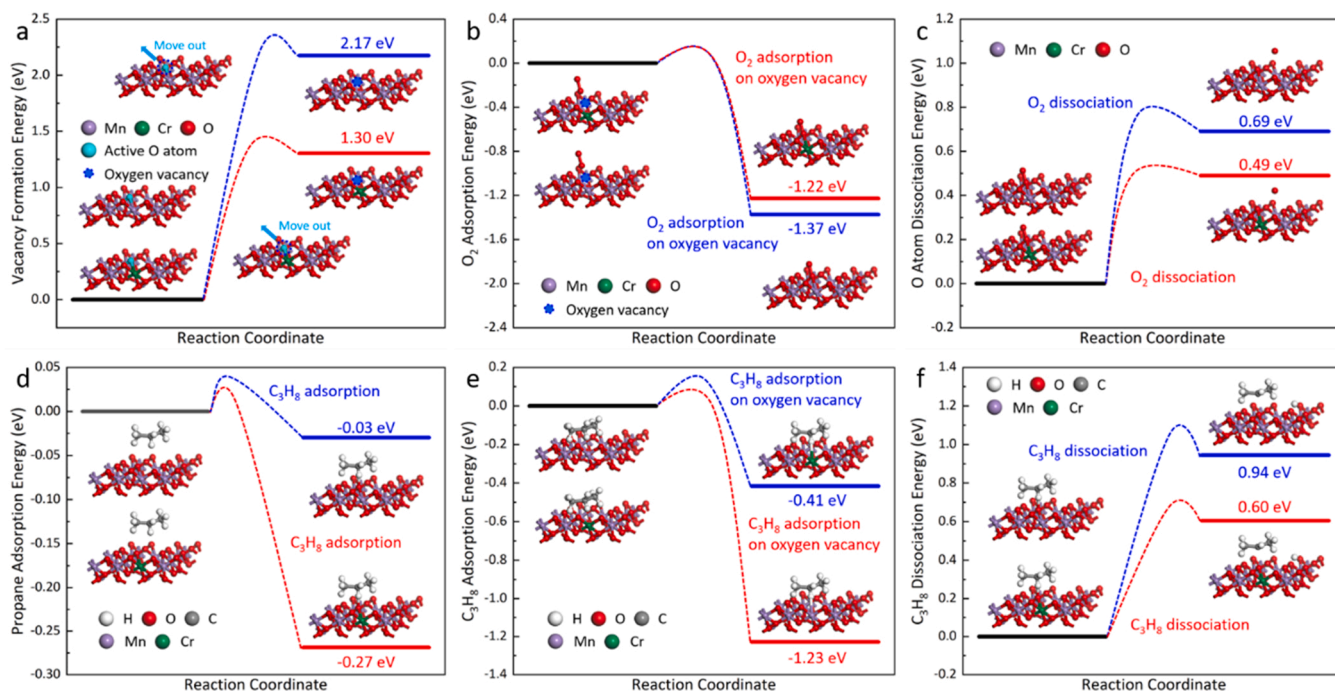


Fig. 9. (a) Oxygen vacancy formation energies, (b) O_2 adsorption energies and (c) O-atom dissociation energy on vacancy of Mn_3O_4 and Mn_3O_4 -Cr catalysts. C_3H_8 adsorption energies on (d) surface and (e) oxygen vacancy of Mn_3O_4 and Mn_3O_4 -Cr. (f) Propane dissociation energies of Mn_3O_4 and Mn_3O_4 -Cr catalyst.

Mn_3O_4 -Cr ($E_{P-Mn_3O_4-Cr} = -2.42$ eV) was closer to E_F ($E_{P-Mn_3O_4} = -2.53$ eV), indicating that electrons could adjust the surface valence state more efficiently and activate the surface adsorbed reactants speedily [49].

Additionally, the adsorption and activation characteristics of Cr-doping were verified by DFT calculation. The oxygen vacancy formation energy (E_v) was calculated to forecast the effect of Cr-doping. E_v values of Mn_3O_4 and Mn_3O_4 -Cr were 2.17 eV and 1.30 eV (Fig. 9a), proving that Cr-doping was conducive to oxygen vacancy formation. When there is oxygen vacancy on surface, the adsorption energy of oxygen molecule decreased from 0.14 eV (Fig. S20) to -1.22 eV (Fig. 9b), indicating that the adsorption form of oxygen molecule changed from physical adsorption to chemical adsorption. Meanwhile, the existence of oxygen vacancy near Cr further strengthened the activation of oxygen molecules on Mn_3O_4 -Cr surface (Fig. 9c, S21) [6,50]. The adsorption energy of propane on Mn_3O_4 surface was -0.03 eV, meaning that propane can only form weak physical adsorption. After Cr doping, the propane adsorption energy decreased to -0.27 eV (Fig. 9d), and further reduced to -1.23 eV, when adsorbed on oxygen vacancies (Fig. 9e). The dissociation energies of propane on surface of Mn_3O_4 and Mn_3O_4 -Cr were 0.94 eV and 0.60 eV (Fig. 9f) separately, indicating that C-H bond were more likely to be catalytically broken on Mn_3O_4 -Cr surface. These strong evidences reveal that Cr-doping enormously reduces the reaction energy barrier and make the propane oxidation more likely to occur.

4. Conclusions

In sum, the Cr element doping method have brought about a vast significant in the propane catalytic performance of the Mn_3O_4 spinel catalysts. $Mn_{2.70}Cr_{0.30}O_4$ displayed the best catalytic activity, stability and resistance. The T_{90} of $Mn_{2.70}Cr_{0.30}O_4$ was 51 °C lower than that of Mn_3O_4 . Characterization and DFT calculation results indicate that Cr-doping was located at the B site of the spinel structure and replaced partly Mn^{3+} . Due to the charge transfer and synergy between Mn and Cr, more high-valence Mn^{4+} species were generated on surface as reaction active sites. Meanwhile, it has been demonstrated that the lattice distortion caused by difference in Cr-O bond length exposed oxygen

vacancies on the surface of $Mn_xCr_{3-x}O_4$, encouraging the adsorption and activation capacity for propane and oxygen molecules. Additionally, in-situ DRIFTS revealed another path with olefin species as the intermediates on $Mn_xCr_{3-x}O_4$ surface, which reduced the energy barrier of oxidative fracture of C-H bond and C-C bond and significantly enhanced the propane oxidation activity. Therefore, Cr element doping strategy is provided with bright prospect for developing efficient VOCs spinel catalysts.

CRediT authorship contribution statement

Chao Feng: Conceptualization, Methodology, Formal analysis, Investigation, Writing – original draft. **Chong Chen:** Validation, Investigation, Data curation. **Gaoyan Xiong:** Validation, Investigation, Data curation. **Di Yang:** Validation, Investigation, Data curation. **Yuan Pan** and **Zhong Wang:** Writing – review & editing, Funding acquisition. **Prof. Zhaoyang Fei:** Writing – review & editing. **Yukun Lu:** Writing – review & editing. **Runduo Zhang:** Writing – review & editing. **Yunqi Liu:** Conceptualization, Resources, Supervision, Writing – review & editing, Funding acquisition. **Xuebing Li:** Conceptualization, Resources, Supervision, Writing – review & editing, Funding acquisition.

Declaration of Competing Interest

The authors declare that they have no known competing financial interests or personal relationships that could have appeared to influence the work reported in this paper.

Data Availability

The data that has been used is confidential.

Acknowledgment

This work was financially supported by the National Natural Science Foundation of China (No. 21878334), the project sanctioned by the Chongqing Science and Technology Bureau (Grant No. cstc2019 jscx-

gksb X0032), the projects sanctioned by the Chongqing Education Commission (Grant No. KJZD-K201800801 and KJZD-M201900802), the State Key Laboratory of Materials-Oriented Chemical Engineering (KL20-09), the Taishan Scholars Program of Shandong Province (No. tsqn201909065), Shandong Provincial Natural Science Foundation (Nos. ZR2021YQ15, ZR2020QB174), Shandong Energy Institute (SEI) (SEI I202109) and the State Key Laboratory of Bio-Fibers and Eco-Textiles of Qingdao University (No. KF2020211).

Notes

The authors declare no competing financial interest.

Appendix A. Supporting information

Supplementary data associated with this article can be found in the online version at doi:10.1016/j.apcatb.2023.122528.

References

- [1] H. Chen, R. Zhang, H. Wang, W. Bao, Y. Wei, Encapsulating uniform Pd nanoparticles in TS-1 zeolite as efficient catalyst for catalytic abatement of indoor formaldehyde at room temperature, *Appl. Catal. B: Environ.* 278 (2020), 119311.
- [2] Q. Song, R. Ran, J. Ding, X. Wu, Z. Si, D. Weng, The controlled preparation and performance of Fe, Co-modified porous ceria nanorods for the total oxidation of propane, *Mol. Catal.* 480 (2020), 110663.
- [3] S. Wu, H. Liu, Z. Huang, H. Xu, W. Shen, O-vacancy-rich porous MnO₂ nanosheets as highly efficient catalysts for propane catalytic oxidation, *Appl. Catal. B: Environ.* 312 (2022), 121387.
- [4] J. Chen, X. Lv, W. Xu, X. Li, J. Chen, H. Jia, Utilizing Cl coordination to facilitate Ru-Ag self-assembling into alloy and recover thermally-inactivated catalyst for propane combustion, *Appl. Catal. B: Environ.* 290 (2021), 119989.
- [5] Y. Guo, M. Wen, G. Li, T. An, Recent advances in VOC elimination by catalytic oxidation technology onto various nanoparticles catalysts: a critical review, *Appl. Catal. B: Environ.* 281 (2021), 119447.
- [6] G. Li, K. He, F. Zhang, G. Jiang, Z. Zhao, Z. Zhang, J. Cheng, Z. Hao, Defect enhanced CoMnNiO_x catalysts derived from spent ternary lithium-ion batteries for low-temperature propane oxidation, *Appl. Catal. B: Environ.* 309 (2022), 121231.
- [7] K. Zeng, Y. Wang, C. Huang, H. Liu, X. Liu, Z. Wang, J. Yu, C. Zhang, Catalytic combustion of propane over MnNbO_x composite oxides: The promotional role of niobium, *Ind. Eng. Chem. Res.* 60 (2021) 6111–6120.
- [8] W. Liao, P. Zhao, B. Cen, A. Jia, J. Lu, M. Luo, Co-Cr-O mixed oxides for low-temperature total oxidation of propane: Structural effects, kinetics, and spectroscopic investigation, *Chin. J. Catal.* 41 (2020) 442–453.
- [9] Y. Jian, M. Tian, C. He, J. Xiong, Z. Jiang, H. Jin, L. Zheng, R. Albilali, J.W. Shi, Efficient propane low-temperature destruction by Co₃O₄ crystal facets engineering: unveiling the decisive role of lattice and oxygen defects and surface acid-base pairs, *Appl. Catal. B: Environ.* 283 (2021), 119657.
- [10] R. Yang, Y. Fan, R. Ye, Y. Tang, X. Cao, Z. Yin, Z. Zeng, MnO₂-based materials for environmental applications, *Adv. Mater.* 33 (2021) 2004862.
- [11] G. Chai, W. Zhang, L.F. Liotta, M. Li, Y. Guo, A. Giroir-Fendler, Total oxidation of propane over Co₃O₄-based catalysts: elucidating the influence of Zr dopant, *Appl. Catal. B: Environ.* 298 (2021), 120606.
- [12] G. Li, N. Li, Y. Sun, Y. Qu, Z. Jiang, Z. Zhao, Z. Zhang, J. Cheng, Z. Hao, Efficient defect engineering in Co-Mn binary oxides for low-temperature propane oxidation, *Appl. Catal. B: Environ.* 282 (2021), 119512.
- [13] Y. Xie, Y. Guo, Y. Guo, L. Wang, W. Zhan, Y. Wang, X. Gong, G. Lu, A highly effective Ni-modified MnO_x catalyst for total oxidation of propane: the promotional role of nickel oxide, *RSC Adv.* 6 (2016) 50228–50237.
- [14] Y. Xie, Y. Guo, Y. Guo, L. Wang, W. Zhan, Y. Wang, X.Q. Gong, G. Lu, A highly-efficient La-MnO_x catalyst for propane combustion: the promotional role of La and the effect of the preparation method, *Catal. Sci. Technol.* 6 (2016) 8222–8233.
- [15] S. Padikkaparambil, S. Sugunan, B.N. Narayanan, Exploration of Mn incorporated CeO₂ nanoflakes with meso- and macropores for the effective simultaneous catalytic oxidation of carbon monoxide and propane, *React. Kinet. Mech. Cat.* 127 (2019) 775–785.
- [16] J. Wang, Y.H. Song, Z.T. Liu, Z.W. Liu, Active and selective nature of supported CrO_x for the oxidative dehydrogenation of propane with carbon dioxide, *Appl. Catal. B: Environ.* 297 (2021), 120400.
- [17] Z. Di, D. Yilmaz, A. Biswas, F. Cheng, H. Leion, Spinel ferrite-contained industrial materials as oxygen carriers in chemical looping combustion, *Appl. Energ.* 307 (2022), 118298.
- [18] C.M. Vladut, S. Mihaiu, O.C. Mocioiu, I. Atkinson, J. Pandele-Cusu, E.M. Anghel, J. M. Calderon-Moreno, M. Zaharescu, Thermal studies of Mn²⁺-doped ZnO powders formation by sol-gel method, *J. Therm. Anal. Calor.* 35 (2019) 2943–2951.
- [19] M. Ghiasse, M. Rezaei, F. Meshkani, S. Mobini, Preparation of the Mn/Co mixed oxide catalysts for low-temperature CO oxidation reaction, *Environ. Sci. Pollut. R.* 28 (2021) 379–388.
- [20] C. Li, D. Brew, J.Y. Lee, Effects of impregnation sequence for Mo-modified V-based SCR catalyst on simultaneous Hg(0) oxidation and NO reduction, *Appl. Catal. B: Environ.* 270 (2020), 118854.
- [21] Z. Huang, S. Yuan, T. Zhang, B. Cai, B. Xu, X. Lu, L. Fan, F. Dai, D. Sun, Selective selenization of mixed-linker Ni-MOFs: NiSe₂@NC core-shell nano-octahedrons with tunable interfacial electronic structure for hydrogen evolution reaction, *Appl. Catal. B: Environ.* 272 (2020), 118976.
- [22] Z. Yang, H. Wang, X. Fei, W. Wang, Y. Zhao, X. Wang, X. Tan, Q. Zhao, H. Wang, J. Zhu, L. Zhou, H. Ning, M. Wu, MOF derived bimetallic CuBi catalysts with ultra-wide potential window for high-efficient electrochemical reduction of CO₂ to formate, *Appl. Catal. B: Environ.* 298 (2021), 120571.
- [23] S. Huang, Y. Wang, S. Qiu, J. Wan, Y. Ma, Z. Yan, Q. Xie, In-situ fabrication from MOFs derived Mn_xCo_{3-x}@C modified graphite felt cathode for efficient electro-fenton degradation of ciprofloxacin, *Appl. Surf. Sci.* 586 (2022), 152804.
- [24] C. Feng, Q. Gao, G. Xiong, Y. Chen, Y. Pan, Z. Fei, Y. Li, Y. Lu, C. Liu, Y. Liu, Defect engineering technique for the fabrication of LaCoO₃ perovskite catalyst via urea treatment for total oxidation of propane, *Appl. Catal. B: Environ.* 304 (2022), 121005.
- [25] C. Wang, X. Du, J. Li, X. Guo, P. Wang, J. Zhang, Photocatalytic Cr(VI) reduction in metal-organic frameworks: A mini-review, *Appl. Catal. B: Environ.* 193 (2016) 198–216.
- [26] Z. Liu, G. Sun, C. Chen, K. Sun, L. Zeng, L. Yang, Y. Chen, W. Wang, B. Liu, Y. Lu, Y. Pan, Y. Liu, C. Liu, Fe-doped Mn₃O₄ spinel nanoparticles with highly exposed Feoct–O–Mntet sites for efficient selective catalytic reduction (SCR) of NO with ammonia at low temperatures, *ACS Catal.* 10 (2020) 6803–6809.
- [27] Y. Zhang, S. Ullah, R. Zhang, L. Pan, X. Zhang, J. Zou, Manipulating electronic delocalization of Mn₃O₄ by manganese defects for oxygen reduction reaction, *Appl. Catal. B: Environ.* 277 (2020), 119247.
- [28] H. Jiang, Z.X. Wei, L. Ma, Y.F. Yuan, J.J. Hong, X.Y. Wu, D.P. Leonard, J. Holoubek, J.J. Razink, W.F. Stickle, F. Du, T.P. Wu, J. Lu, X. Ji, An aqueous dual-ion battery cathode of Mn₃O₄ via reversible insertion of nitrate, *Angew. Chem. Int. Ed.* 58 (2019) 5286–5291.
- [29] S. Zhang, H. Li, Z. Wu, J.E. Post, B. Lanson, E.J. Elzinga, Y. Liu, H. Li, M. Hong, F. Liu, H. Yin, Effects of Co doping on the structure and physicochemical properties of hausmannite (Mn₃O₄) and its transformation during aging, *Chem. Geol.* 582 (2021), 120448.
- [30] B. Sarkar, P. Prajapati, R. Tiwari, R. Tiwari, S. Ghosh, S.S. Acharyya, C. Pendem, R. K. Singha, L.N. Sivakumar Konathala, J. Kumar, T. Sasakib, R. Bal, Room temperature selective oxidation of cyclohexane over Cu-nanoclusters supported on nanocrystalline Cr₂O₃, *Green. Chem.* 14 (2012) 2600.
- [31] E. Gao, G. Sun, W. Zhang, M.T. Bernards, Y. He, H. Pan, Y. Shi, Surface lattice oxygen activation via Zr⁴⁺ cations substituting on A²⁺ sites of MnCr₂O₄ forming Zr_xMn_{1-x}Cr₂O₄ catalysts for enhanced NH₃-SCR performance, *Chem. Eng. J.* 380 (2020), 122397.
- [32] Y. Jian, X. Feng, M. Tian, Z. Jiang, C. He, Birnessite-type short rod-like MnO₂ achieving propane low-temperature destruction: Benign synthesis strategy and reaction mechanism determination, *Appl. Surf. Sci.* 559 (2021), 149905.
- [33] C. Feng, G. Xiong, F. Jiang, Q. Gao, C. Chen, Y. Pan, Z. Fei, Y. Li, Y. Lu, C. Liu, Y. Liu, Assembly of sphere-structured MnO₂ for total oxidation of propane: structure-activity relationship and reaction mechanism determination, *Sep. Purif. Technol.* 284 (2022), 120269.
- [34] P. Li, Y. Lin, S. Zhao, Y. Fu, W. Li, R. Chen, S. Tian, Defect-engineered Co₃O₄ with porous multishelled hollow architecture enables boosted advanced oxidation processes, *Appl. Catal. B: Environ.* 298 (2021), 120596.
- [35] M. Setvin, U. Aschauer, P. Scheiber, Y.F. Li, W. Hou, M. Schmid, A. Selloni, U. Diebold, Reaction of O₂ with subsurface oxygen vacancies on TiO₂ anatase (101), *Science* 341 (2013) 988–991.
- [36] J. Li, B. Liu, J. Dong, C. Li, Q. Dong, T. Lin, R. Liu, P. Wang, P. Shen, Q. Li, B. Liu, Size and morphology effects on the high pressure behaviors of Mn₃O₄ nanorods, *Nanoscale Adv.* 2 (2020) 5841–5847.
- [37] X. Hou, G.Q. Xiao, D.H. Ding, N.X. Zhang, Y.Q. Gao, Effects of Cr₂O₃ content on viscosity and microstructure of copper converter slag, *J. Non-Cryst. Solids* 574 (2021), 121147.
- [38] H. Liu, W. Jia, X. Yu, X. Tang, X. Zeng, Y. Sun, T. Lei, H. Fang, T. Li, L. Lin, Vitamin C-assisted synthesized Mn–Co oxides with improved oxygen vacancy concentration: Boosting lattice oxygen activity for the air-oxidation of 5-(Hydroxymethyl)furfural, *ACS Catal.* 11 (2021) 7828–7844.
- [39] L. Kang, B. Wang, Q. Bing, M. Zalibera, R. Büchel, R. Xu, Q. Wang, Y. Liu, D. Gianolio, C.C. Tang, E.K. Gibson, M. Danaie, C. Allen, K. Wu, S. Marlow, L. D. Sun, Q. He, S. Guan, A. Savitsky, J.J. Velasco-Vélez, J. Callison, C.W.M. Kay, S. E. Pratsinis, W. Lubitz, J.Y. Liu, F.R. Wang, Adsorption and activation of molecular oxygen over atomic copper(I/II) site on ceria, *Nat. Commun.* 11 (2020) 4008.
- [40] X. Yu, M. Shi, Y. Fan, L. Yang, J. Zhang, W. Liu, W. Dai, S. Zhang, L. Zhou, X. Luo, S. Luo, Activation or passivation: Influence of halogen dopant (F, Cl, Br) on photochemical activity of Mn₂O₃ in degrading toluene, *Appl. Catal. B: Environ.* 309 (2022), 121236.
- [41] S. Xiong, Y. Peng, D. Wang, N. Huang, Q. Zhang, S. Yang, J. Chen, J. Li, The role of the Cu dopant on a Mn₃O₄ spinel SCR catalyst: Improvement of low-temperature activity and sulfur resistance, *Chem. Eng. J.* 387 (2020), 124090.
- [42] J. Shi, H. Li, A. Genest, W. Zhao, P. Qi, T. Wang, G. Rupprechter, High-performance water gas shift induced by asymmetric oxygen vacancies: Gold clusters supported by ceria-praseodymia mixed oxides, *Appl. Catal. B: Environ.* 301 (2022), 120789.
- [43] C. Feng, F. Jiang, G. Xiong, C. Chen, Z. Wang, Y. Pan, Z. Fei, Y. Lu, X. Li, R. Zhang, Y. Liu, Revelation of Mn⁴⁺-O_{sur}-Mn³⁺ active site and combined Langmuir-Hinshelwood mechanism in propane total oxidation at low temperature over MnO₂, *Chem. Eng. J.* 451 (2023), 138868.

- [44] Z. Zhao, T. Wu, C. Xiong, G. Sun, R. Mu, L. Zeng, J. Gong, Hydroxyl-mediated non-oxidative propane dehydrogenation over $\text{VO}_x/\gamma\text{-Al}_2\text{O}_3$ catalysts with improved stability, *Angew. Chem. Int. Ed.* 57 (2018) 6791–6795.
- [45] W. Zhu, X. Chen, C. Li, Z. Liu, C. Liang, Manipulating morphology and surface engineering of spinel cobalt oxides to attain high catalytic performance for propane oxidation, *J. Catal.* 396 (2021) 179–191.
- [46] J. Duan, L. Zhao, S. Gao, Y. Zhang, Reaction mechanism of H_2 -assisted C_3H_6 -SCR over Ag-Ce_xZr catalyst as investigated by in situ FTIR, *Chem. Res. Chin. U* 36 (2020) 885–893.
- [47] Z. Hu, Y. Wang, D. Yang, Z.Y. Yuan, CrO_x supported on high-silica HZSM-5 for propane dehydrogenation, *J. Energy Chem.* 47 (2020) 225–233.
- [48] X. Zou, L. Wang, X. Ai, H. Chen, X. Zou, Crystal phase-dependent electrocatalytic hydrogen evolution performance of ruthenium-boron intermetallics, *Chem. Commun.* 56 (2020) 3061–3064.
- [49] K. Chu, Y. Liu, Y. Li, Y. Guo, Y. Tian, H. Zhang, Multi-functional Mo-doping in MnO_2 nanoflowers toward efficient and robust electrocatalytic nitrogen fixation, *Appl. Catal. B: Environ.* 264 (2020), 118525.
- [50] Z. Zhao, G. Li, Y. Sun, N. Li, Z. Zhang, J. Cheng, C. Ma, Z. Hao, The positive effect of water on acetaldehyde oxidation depended on the reaction temperature and MnO_2 structure, *Appl. Catal. B: Environ.* 303 (2022), 120886.